

The Mechanism of Cavitation-Induced Scission of Single-Walled Carbon Nanotubes

Frank Hennrich,^{*,†} Ralph Krupke,^{‡,§} Katharina Arnold,[†] Jan A. Rojas Stütz,[§]
Sergei Lebedkin,[†] Thomas Koch,^{†,||} Thomas Schimmel,^{†,||} and Manfred M. Kappes^{†,§}

Forschungszentrum Karlsruhe, Institut für Nanotechnologie, D-76021 Karlsruhe, Germany,
Physikalisches Institut, Universität Karlsruhe, D-76128 Karlsruhe, Germany, Institut für Physikalische Chemie,
Universität Karlsruhe, D-76128 Karlsruhe, Germany, and Institut für Angewandte Physik,
Universität Karlsruhe, D-76128 Karlsruhe, Germany

Received: August 15, 2006; In Final Form: November 16, 2006

Aqueous suspensions of length selected single-walled carbon nanotubes were studied by atomic force microscopy (AFM) in order to probe the influence of sonication on nanotube scission. The maximum of the tube length distribution, l_M , initially exhibits a power law dependence on the sonication time, t — roughly as $l_M \approx t^{-0.5}$. This and the limiting behavior observed at longer times can be rationalized to first order in terms of a continuum model deriving from polymer physics. In this picture, the strain force associated with cavitation scales with the square of the nanotube length. Scission stops when the strain force falls below the critical value for nanotube disruption.

Introduction

Several methods have been developed to sort liquid-suspended single-walled carbon nanotubes (SWNTs) by length, including capillary electrophoresis,^{1,2} gel electrophoresis,^{3,4} liquid–liquid extraction,⁵ and size-exclusion chromatography.^{6–10} Heller et al. have recently inferred that gel electrophoresis and size-exclusion chromatography conducted on individually dispersed SWNTs subjected to an (additional) ultrasound treatment yield a simultaneous separation by tube length and diameter.⁴ They have rationalized their observations in terms of a diameter-dependent sonication-induced scission rate which would give rise to shorter nanotube fractions enriched in large diameter tubes, whereas longer nanotube fractions are enriched in small diameter tubes.

In order to further explore such sonication-induced, diameter-selective cutting processes, it is necessary to study the underlying mechanism. Sonication has already been used by several researchers for cutting SWNTs into shorter pieces in combination with strong acids¹¹ or together with additives such as diamond,¹² polymers,¹³ or DNA.¹⁴ In a study aimed at improving the solubilization of SWNTs in aqueous media, Islam et al.¹⁵ have examined the surfactant dependence of suspension efficiency and have optimized the conditions for fragmentation-free ultrasonic dispersion (high frequency, low power). These authors were the first to investigate the efficacy of SWNT suspension schemes by using atomic force microscopy (AFM) measurements of spin-coated material to determine SWNT diameter and length distributions in the corresponding suspensions. In the present study, we have used this approach in combination with length fractionation by size-exclusion chromatography to provide a systematic measure of the influence of ultrasonic treatment on SWNT scission. Length-dependent scission rates are interpreted to first order in terms of a continuum physics approach

originally developed to describe scission of polymer chains. This allows insight into the mechanism of water-cavitation-induced scission of SWNTs.

Experimental Section

Two different SWNT materials were used for this study: (i) SWNT soot produced by the HiPco method¹⁶ and obtained from Rice University and (ii) SWNT soot produced by a variant¹⁷ of the pulsed laser vaporization (PLV) method.¹⁸ Specifically, PLV SWNT soot was generated using graphite targets doped with 1 atom % Ni and Co (Toyo Tanso) in an Ar gas flow at an oven temperature of 1000 °C. Prior to further use, the PLV SWNT soot was purified by washing it three times with dimethylformamide (DMF) according to ref 19. The HiPco material was used as received.

Length selected SWNTs for further study were prepared by size-exclusion chromatographic fractionation of suspensions of the SWNT starting materials. For this, 15 mg of the SWNT material was first suspended in 30 mL of D₂O with 1 wt % sodium cholate (Sigma Aldrich) using a tip sonicator (Bandelin, 200 W maximum power, 20 kHz) applied for 1 h at 10% power while cooling the sample in an ice bath. After centrifugation at 20 000g to remove larger agglomerates, the resulting suspension was then fractionated without further treatment. Size-exclusion chromatography was performed with a Sephacryl S-500 gel filtration medium (Amersham Biosciences) in a glass column of 120 cm length and 1 cm inner diameter. After filling the glass column with the filtration medium, the gel was slightly compressed to yield a final height of 100 cm. For the size separation, 4 mL of SWNT suspension (2 mg of SWNTs) was applied to the top of the column and a solution of 1 wt % sodium cholate in D₂O as eluant was pushed through the column by applying sufficient pressure with compressed air to ensure a flow of ~1 mL/min. Fractions were collected in 2 mL portions.

For the scission study, 2 mL of a fraction with known length distribution was diluted by a factor of 10 with a 1 wt % sodium cholate D₂O solution and sonicated for 2 h. Aliquots for AFM study were taken after 5, 10, 40, 60, 90, and 120 min.

* Corresponding author. E-mail: Frank.Hennrich@int.fzk.de.

† Institut für Nanotechnologie.

‡ Physikalisches Institut, Universität Karlsruhe.

§ Institut für Physikalische Chemie, Universität Karlsruhe.

|| Institut für Angewandte Physik, Universität Karlsruhe.

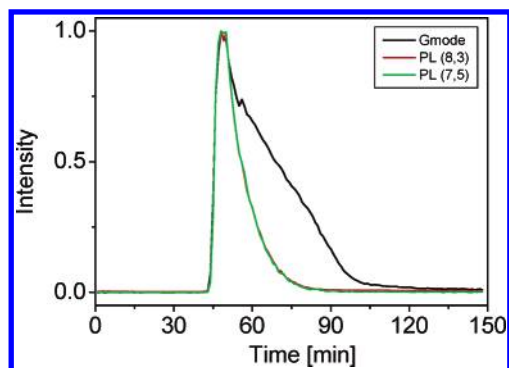


Figure 1. Chromatogram derived from a size-exclusion fractionation using HiPco SWNTs in D₂O and 1 wt % sodium cholate on Sephacryl S-500 gel.

Raman spectra at 785 nm excitation were obtained directly at the outlet of the glass size-exclusion column with a Kaiser Optical HoloSpec spectrograph which comprises a fiber optic probe head incorporating both excitation laser aperture and collection optics. Spectra were processed via the Kaiser HoloReact program package for Matlab (The Mathworks, Inc.). Peak heights of Raman and fluorescence features were calculated at defined wavelength intervals over each spectrum taken. These were typically recorded every minute during the size-exclusion experiment. The RBM region between 150 and 300 cm⁻¹ can be fitted by Lorentzian functions and assigned to SWNTs with distinct n and m according to ref 20: (12, 5), (13, 3), (9, 8), (14, 1), (9, 7), (10, 5), (11, 3), (12, 1), and (11, 0). The additional fluorescence peak detected in the case of the HiPco material can be assigned to SWNTs with distinct n and m according to ref 21.

AFM samples were prepared by spin coating of the nanotube suspensions onto silicon wafers and rinsing with water and acetone. Intermittent contact mode²² AFM images were taken with a Digital Instruments Multimode SPM with NSC15 silicon cantilevers (MikroMasch). The heights and lengths of the measured objects were extracted from AFM images with the help of the Software package SIMAGIS (Smart Imaging Technologies Co.). Tube lengths were determined within a lateral resolution of 10–20 nm.^{22,23}

Two-dimensional photoluminescence (PL) contour maps of size separated tube samples in surfactant solutions were derived from individual PL emission spectra measured in the range 850–1750 nm with a similar setup and procedures as already described in ref 24 using a Fourier transform (FT) IR technique (Bruker IFS66) for detection and a monochromatized light source (Xenon lamp) for the excitation in the range 500–860 nm. UV–vis–NIR absorption spectra of eluting fractions were recorded on a Varian Cary 500 spectrophotometer. For better comparison, a background was subtracted from all spectra. The background was generated by a spline fit for one representative spectrum and was then applied to all other spectra.

Results

Figure 1 shows typical chromatograms obtained by plotting normalized peak height intensities of the Raman G mode and normalized peak height intensities (normalized to the maximum signal in each) of fluorescence features for (8, 3) and (7, 5) tubes against time. Fractions were cut within the broad peak between 40 and 100 min. Note that as we use only Raman/fluorescence spectra as the online detection method to follow tube motion through the gel (resonant with only ~10 different n,m), it is conceivable that results may not be representative

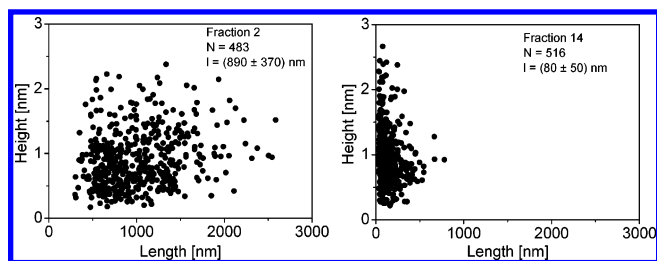


Figure 2. Length and height distribution of fractions 2 and 14 from size-exclusion chromatography of HiPco SWNTs in D₂O and 1 wt % sodium cholate on Sephacryl S-500 gel obtained from the analysis of intermittent contact mode AFM images.

for the whole n,m distribution. In the following discussion, we assume that this is not an issue.

In AFM measurements of fractions deriving from the starting suspension, we examined ~500 tubes or small bundles for each of five different fractions. As an example, Figure 2 provides a summary of the AFM observations for fractions 2 and 14. The mean length of the examined fractions is as follows: 890 ± 370 nm for fraction 2, 520 ± 235 nm for fraction 5, 230 ± 110 nm for fraction 8, 140 ± 80 nm for fraction 11, and 80 ± 50 nm for fraction 14. In the AFM measurements of the scission process, ~500 tubes or small bundles were typically also probed so as to obtain a statistical sampling.

PL intensities measured for nanotube samples do not reflect the relative abundance of nanotube chiralities because (i) metallic tubes do not photoluminesce and (ii) associated cross sections are predicted to be strongly dependent on the chiral vector but are not accurately known (and may also be length dependent).²⁵ Nevertheless, PL maps can at least be used to qualitatively compare the effects of different sample treatments for the same nanotube starting material. In Figure 3, the PL contour maps of fractions 2 and 15 are shown. Comparing these maps, it appears that there is more PL intensity for tubes with smaller diameters in the 890 nm average length sample than is the case for the 80 nm fraction. This observation is analogous to what was found by Heller et al., who have interpreted this behavior in terms of a diameter-dependent sonication-induced “cutting” rate.⁴

Figure 4 shows UV–vis–NIR absorption spectra for various fractions. The peaks from interband transitions all seem to lie on the same background but become weaker with increasing elution time. This might be explained by the fact that cross sections for interband transitions are length dependent or may simply be due to the fact that side products from the SWNT synthesis such as amorphous carbon are also separated by size (and come off the column after a certain time). The background corrected spectra show length-fraction-dependent changes in intensity ratios between different peaks in the S1 region and some minor changes in peak intensities in the S2 region. These follow the same qualitative trend as already described for the PL contour maps but are not in quantitative agreement. Note that part of the discrepancy is due to an intrinsic difference between UV–vis–NIR and PL measurements. In PL, only those individualized tubes contribute significantly to the emission spectra, which are not associated in bundles. In the UV–vis–NIR spectra, individual tubes and tubes in bundles contribute to spectra. Interestingly, we do not see changes in height profiles extracted from AFM measurements for the various length fractions. Mean heights of all fractions are in the range 0.8 ± 0.3 nm, which is consistent with either an individual tube or a bundle of two or at most three tubes (which cannot be really distinguished from a single tube with Intermittent contact mode

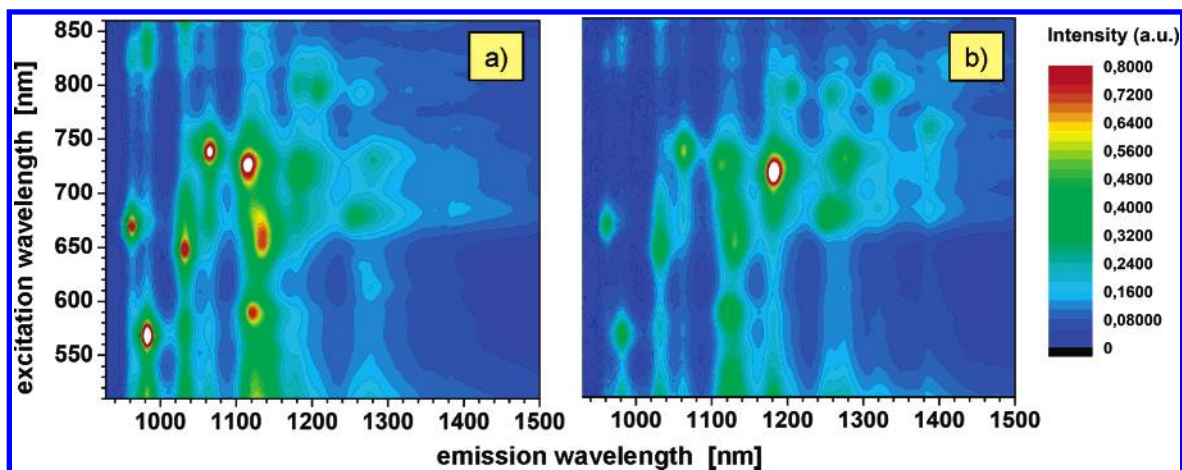


Figure 3. PL contour maps of (a) fraction 2 and (b) fraction 15. The spectra are normalized to the nanotube with highest relative intensity.

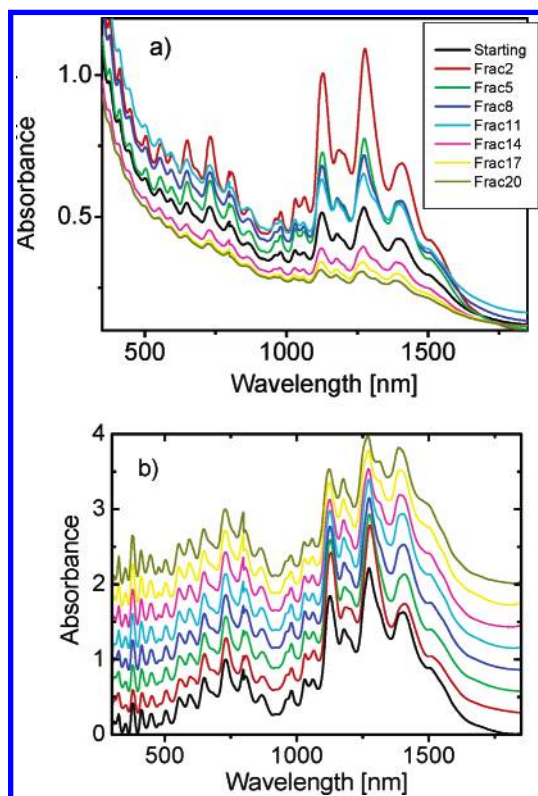


Figure 4. UV-vis-NIR absorption spectra of several fractions. In part b, the spectra are background corrected, normalized to the peak at 1125 nm, and vertically shifted for better comparison.

AFM). We could not identify any length fractions having a significant content of larger bundles.

To further study the scission process, we sonicated a fraction of PLV tubes with known length distribution for 2 h and analyzed it with AFM after 5, 10, 40, 60, 90, and 120 min. Figure 5 contains the length distributions extracted from the AFM images. The starting PLV tube fraction had a mean length of 800 ± 300 nm, and after sonication for 5, 10, 40, 60, 90, and 120 min, the tubes had a length distribution of 560 ± 270 , 240 ± 240 , 200 ± 195 , 240 ± 130 , 205 ± 110 , and 165 ± 80 nm. These observations show that the tubes are effectively cut by sonication. After 40 min, 800 ± 300 nm long tubes have been cut down to a length of ~ 200 nm. Furthermore, measurements taken at longer times show that after ~ 40 min the scission process has essentially come to a halt. While the mean length remains roughly constant, the statistical distribution continues to become narrower.

Sonication experiments on polymers have established that ultrasound treatment can effectively cut polymers into shorter chains.^{26,27} The effect arises from cavitation bubbles, which generate high strain rates in the surrounding liquid upon implosion. Friction forces between the moving liquid and the polymer stretch the polymer and can eventually lead to bond fracture if the load is high enough. We suggest that a similar scission mechanism is causing nanotube shortening under sonication. Next, we discuss a simple continuum model based on this picture which provides a qualitative description of the evolution of the nanotube length distribution under sonication.

The strain rate, $d\epsilon/dt$, which depends on the bubble dynamics, can be calculated from the distance, r , to the center of the cavity, the bubble radius, R , and the bubble wall velocity, dR/dt ²⁸:

$$\frac{d\epsilon}{dt} = -2 \frac{R^2}{r^3} \frac{dR}{dt} \quad (1)$$

The bubble dynamics, modeled on the basis of the Rayleigh–Plesset equation, depends on the surface tension, the vapor pressure, the liquid viscosity, the static pressure, and the acoustic pressure. For water under ambient conditions, being sonicated with an ultrasound frequency, f , of 20 kHz and at an acoustic pressure, P_A , of 10 bar, the strain rate, $d\epsilon/dt$, close to a collapsing bubble can be as large as 10^9 s^{-1} . The nanotube, treated as a rigid entity, will move with the fluid at a velocity up to 2500 m/s. However, due to the radial velocity profile, there must be a relative motion between molecule and fluid of varying sign and magnitude for different points along the nanotube. An exception is the midpoint, which will follow the surrounding liquid (Figure 6). Due to a frictional force between the fluid and the various points along the nanotube in relative motion, it follows that the tube will be under tension with the maximum of the stress in the center. If the stress exceeds the maximum stress a nanotube can tolerate, then the tube will break.

Stokes' law expresses the above forces quantitatively. Keller and Rubinow²⁹ have shown that the drag force, F , on a circular cylinder of length L and diameter a moving as a rigid body parallel to its long axis in a fluid is given by

$$F = 2\pi\mu LV \left\{ \left[\log \frac{L}{a} - \frac{3}{2} + \log 2 - \left(1 - \frac{\pi^2}{12} \right) \log \frac{L}{a} \right]^{-1} + O\left[\left(\frac{1}{\log L/a} \right)^4 \right] \right\} \quad (2)$$

with V being the relative velocity between cylinder and fluid and μ being the viscosity of the fluid.

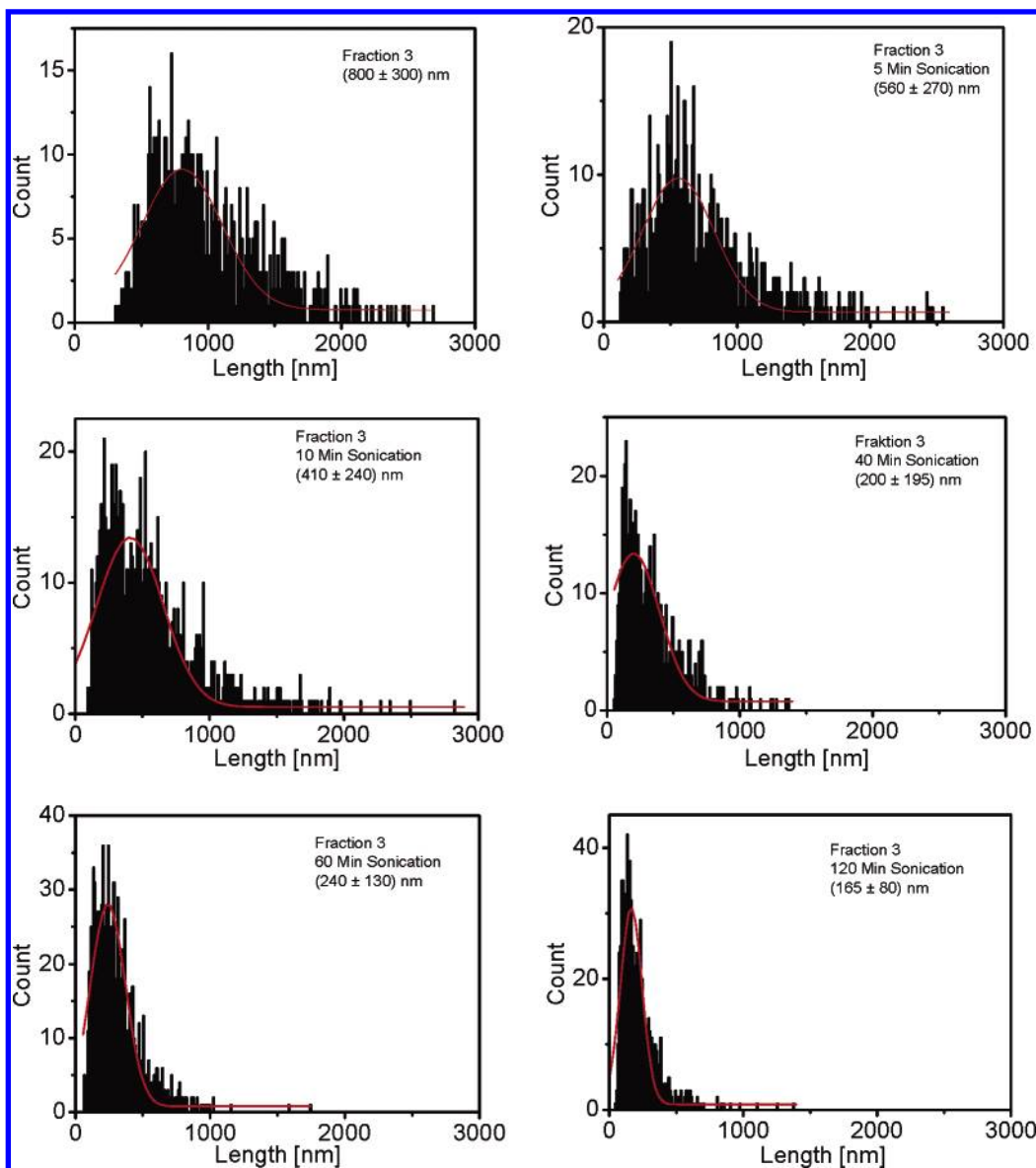


Figure 5. Length statistics extracted from AFM images taken from samples with PLV tubes of a mean length of 800 nm (± 300 nm standard deviation) after sonication for 5, 10, 40, 60, and 120 min.

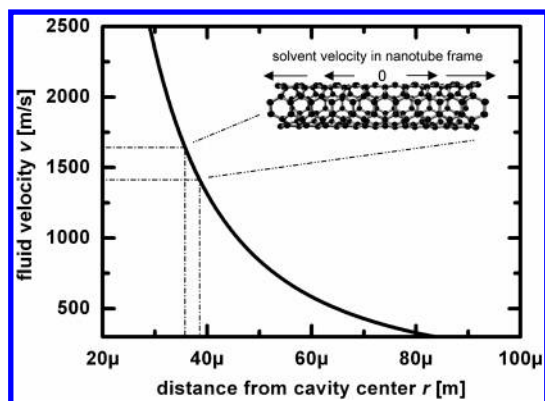


Figure 6. Illustration of a carbon nanotube in a radial flow field and the resulting relative solvent velocity. The fluid velocity, v , versus distance, r , from the cavity center is shown close to an imploding bubble in water under ambient conditions for a 20 μm bubble, driven at 20 kHz and an acoustic pressure of 10 bar. The data are based on numerical results from ref 32.

For our nanotubes with a typical diameter of $a \approx 1\text{--}1.4$ nm and length of $L \approx 100\text{--}1000$ nm, the logarithmic corrections in brackets are of the order of 1.

To derive the forces within a nanotube caused by the velocity gradient along the nanotube, we express the relative velocity, V , as a function of the distance, x , from the nanotube center by $V(x) = \dot{\epsilon} \cdot x$, where the elongational strain rate, $d\epsilon/dt$, is given by $\dot{\epsilon} = v_X/x$. We then cut a tube virtually into segments and define a force per unit length, f , as $f = 2\pi\mu V$ by assuming the logarithmic corrections are independent of the virtual nanotube length.

The force per unit length along the nanotube is then given by

$$f(x) = 2\pi\mu\dot{\epsilon}x \quad (3)$$

To calculate the net force at the nanotube center, F_M , we need to integrate the absolute value of $f(x)$ from $-L/2$ to $+L/2$ and obtain

$$F_M = \frac{1}{2} \pi\mu\dot{\epsilon}L^2 \quad (4)$$

The important result of eq 4 is the dependence of F_M on the squared nanotube length, the strain rate, and the fluid viscosity,

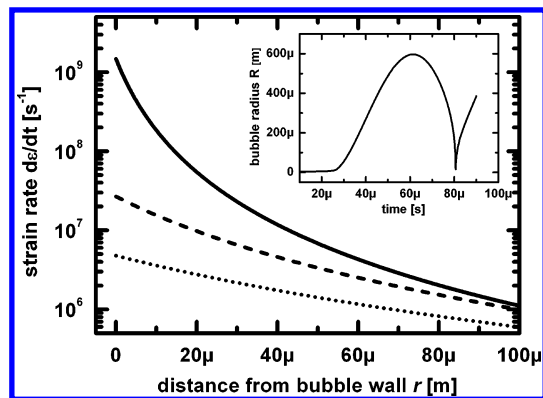


Figure 7. Strain rate, $\dot{\epsilon}$, versus distance from bubble wall, r , for a bubble radius of 10 μm (—), 50 μm (---), and 100 μm (····) calculated with eq 4 based on the data from ref 32. The insert illustrates bubble growth and implosion dynamics.

which together determine the evolution of the length distribution toward the terminal length, L_T .

After long sonication time, most of the tubes have been shortened to L_T with the corresponding $F_M(L_T)$ being comparable to or smaller than the force, F_C , needed for nanotube disruption. The tensile stress, P_C , of a SWNT is ~ 80 GPa.³⁰ For a SWNT with a diameter of $d = 1.2$ nm and a wall thickness of $w = 0.34$ nm,³⁰ we obtain $F_C = P_C(\pi(2dw - w^2)/4) \approx 44$ nN as the force for nanotube disruption.

From eq 4, we can now calculate the maximum strain rate, $\dot{\epsilon}$, needed to cut tubes to the experimentally observed terminal length, $L = L_T \approx 100$ nm, using $F_M = F_C$ and $\mu = 10^{-3}$ Pa s for the viscosity of water. We obtain $\dot{\epsilon} = 10^9$ s $^{-1}$, a value which is in reasonable agreement with the strain rate derived from the numerical modeling of the bubble dynamics (Figure 7).

We note that the application of a continuum model to a nanoscale object may not be appropriate. However, Walther³¹ has recently shown by molecular dynamics modeling that the drag coefficient for a nanotube in a perpendicular fluid flow at comparable relative flow velocity can indeed be well described by a continuum Navier–Stokes model. Molecular dynamics calculations for fluid flow parallel to the nanotube axis are unfortunately not available.

We next calculate the time evolution of the nanotube length distribution by modeling the scission kinetics based on the starting experimental length distribution. For this, we take the rate, k , for scission of a tube of original length L_n into the two tube segments L_m and L_{n-m} as

$$k(L_n, L_m) = c \frac{L_n^\alpha}{\sqrt{2\pi}\sigma} \exp\left(-\frac{1}{2\sigma^2}\left(L_m - \frac{L_n}{2}\right)^2\right) \quad (5)$$

The scission rate, k , is a product of the dependence on L_n to the power of $\alpha \approx 2$ and of a Gaussian distribution function which allows for the nonrandom scission process into two (nearly complementary) tube segments with a Gaussian width, σ , similar to the model of polymer cutting.²⁷ c is a proportionality constant. Recombination of tube segments is not considered. The scission rate model takes into account the predicted square dependence of the force F_M on the length, L (eq 4), but not the anticipated $k(L_n < L_T) = 0$ dependence, which determines the final length distribution. This may cause deviations of our calculation from the experimental data for very long sonication times.

The population balance is then given by

$$\frac{dP(L_n)}{dt} = \sum_{L_m > L_n} k(L_m, L_n) P(L_m) - P(L_n) \sum_{L_m=0}^{L_n} k(L_n, L_m) \quad (6)$$

with the probabilities P_n and P_m to find a nanotube with lengths L_n and L_m , respectively.

On the basis of eqs 5 and 6, we have calculated the evolution of the length distribution by fitting α , σ , and c to the experimental data, starting with the experimental data at $t = 0$ s. Figure 8 shows the results of the simulation normalized to the maximum of each length distribution, as the number of nanotubes is not preserved due to cutting. The distributions were recalculated with a time interval of 15 ms at $c = 10^{-2}$ starting with the experimentally determined initial length distribution. Within the experimental error, we have found a best fit to the measured evolution of length distribution with $\alpha = 1.8$ and $\sigma = 0.6$ nm.

Figure 9 shows the evolution of the length distribution. The calculated maximum of the length distribution, I_M , exhibits a power law dependence on the sonication time, t , which scales as $I_M \approx t^{-0.5}$. The experimental values are in reasonable agreement with this predicted trend. We attribute pronounced deviations at short sonication times to a convolution of the nanotube cutting with the process of debundling.

We note that for the sake of simplicity our kinetic model does not include a dependence of the cutting rate on the nanotube diameter. On the other hand, the continuum model predicts a nonlinear diameter dependence of drag force, F (eq 2), which does not quite compensate for the expected linear dependence of the disruption force, F_C , on tube diameter. In Figure 10 are plotted the logarithmic corrections of eq 2 (in bracket terms: g) versus the nanotube diameter, a , for various tube lengths, L . The data can be fitted to a power law dependence of $g \sim a^\alpha$, with α being equal to 0.52, 0.64, 0.91, 1.36, and 1.83 for tubes with L equal to 1 μm , 500 nm, 200 nm, 100 nm, and 70 nm, respectively. Since the force needed to disrupt a nanotube depends linearly on the diameter, we in fact expect a small diameter dependence on the cutting process for all L with $\alpha \approx 1$.

Note, however, that a larger diameter dependence might arise from various effects not considered in the continuum model such as

(i) Modifications to the drag forces due to SWNT surfactant coating. In our approach, we considered the tubes only to be surrounded by water.

(ii) Tube bundling. Most tubes are probably still associated with one other tube or two other tubes in very small bundles. Consequently, diameter-selective cutting might simply reflect easier disengagement of larger diameter tubes from bundles than small diameter tubes. As a result, the more readily individualized larger tubes might then be cut faster than the small diameter tubes.

(iii) Defects. We have not taken into account that tubes probably contain significant defect densities. Tube scission is likely to preferentially commence at such defect sites. Conceivably, larger diameter tubes have more defects per length than smaller diameter tubes.

Additionally, it is likely that absorption and fluorescence cross sections depend nonlinearly on tube length (in particular for short tube segments). We intend to explore these issues in more detail in future work.

In conclusion, we have carried out experiments and modeling which allow the establishment of a first-order mechanistic picture for how length selected SWNTs are cut by sonication

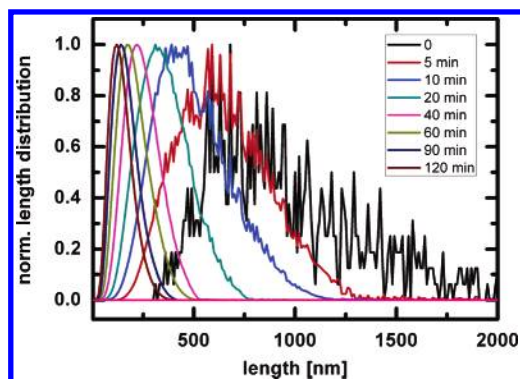


Figure 8. Normalized length distribution calculated from the experimentally determined initial distribution ($t = 0$).

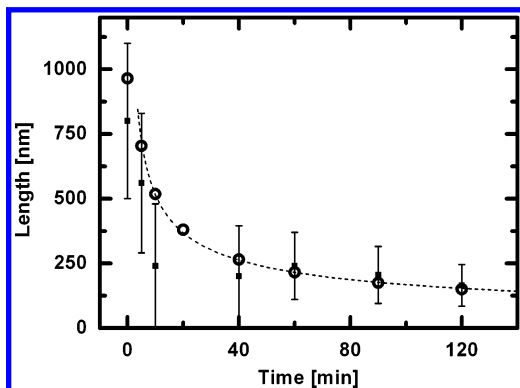


Figure 9. Maximum of length distribution versus sonication time. The maximum of the measured distribution (■) is compared with the calculated distribution (○). A best fit to the calculated distribution (---) yields a dependence on time to the power of -0.49 .

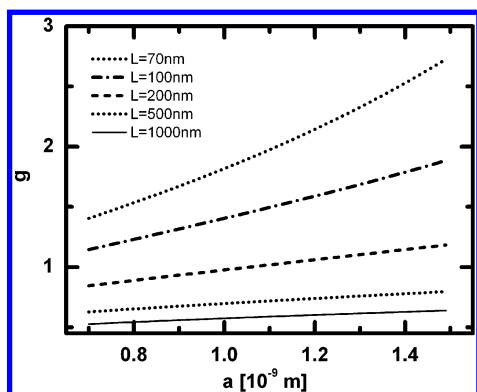


Figure 10. Logarithmic correction, g , of eq 2 plotted versus nanotube diameter, a , for various tube lengths.

in aqueous surfactant suspensions. The maximum of the tube length distribution, l_M , exhibits a roughly power law dependence on the sonication time, t , with $l_M \approx t^{-0.5}$. The associated limiting behavior can be rationalized in terms of a continuum model where the strain force associated with cavitation scales with the square of the nanotube length. Scission stops when the strain force falls below the critical value for nanotube disruption.

Acknowledgment. R.K. acknowledges F. Evers for discussions and the Initiative and Network Fund of the Helmholtz-Gemeinschaft Deutscher Forschungszentren (HGF) for funding.

M.M.K. acknowledges partial funding by the Deutsche Forschungsgemeinschaft.

Supporting Information Available: AFM images of fractions 14 and 2. This material is available free of charge via the Internet at <http://pubs.acs.org>.

References and Notes

- (1) Doorn, S. K.; Fields, R. E., III; Hu, H.; Hamon, M. A.; Haddon, R. C.; Selegue, J. P.; Majidi, V. J. *Am. Chem. Soc.* **2002**, *124*, 3169–3174.
- (2) Doorn, S. K.; Strano, M. S.; O'Connell, M. J.; Haroz, E. H.; Rialon, K. L.; Hauge, R. H.; Smalley, R. E. *J. Phys. Chem. B* **2003**, *107*, 6063–6069.
- (3) O'Connell, M. J.; Boul, P.; Ericson, L. M.; Huffman, C.; Wang, Y.; Haroz, E.; Kuper, C.; Tour, J.; Ausman, K. D.; Smalley, R. E. *Chem. Phys. Lett.* **2001**, *342*, 265–271.
- (4) Heller, D. A.; Mayrhofer, R. M.; Baik, S.; Grinkova, Y. V.; Usrey, M. L.; Strano, M. S. *J. Am. Chem. Soc.* **2004**, *126*, 14567–14573.
- (5) Ziegler, K. J.; Schmidt, D. J.; Rauwald, U.; Shah, K. N.; Flor, E. L.; Hauge, R. H.; Smalley, R. E. *Nano Lett.* **2005**, *5*, 2355–2359.
- (6) Duesberg, G. S.; Muster, J.; Krstic, V.; Burghard, M.; Roth, S. *Appl. Phys. A* **1998**, *67*, 117–119.
- (7) Chattopadhyay, D.; Lastella, S.; Kim, S.; Papadimitrakopoulos, F. *J. Am. Chem. Soc.* **2002**, *124*, 728–729.
- (8) Niyogi, S.; Hu, H.; Hamon, M. A.; Bhowmik, P.; Zhao, B.; Rozentzhak, S. M.; Chen, J.; Itkis, M. E.; Meier, M. S.; Haddon, R. C. *J. Am. Chem. Soc.* **2001**, *123*, 733–734.
- (9) Farkas, E.; Anderson, M. E.; Chen, Z.; Rinzler, A. G. *Chem. Phys. Lett.* **2002**, *363*, 111–116.
- (10) Huang, X.; Mclean, R. S.; Zheng, M. *Anal. Chem.* **2005**, *77*, 6225–6228.
- (11) Liu, J.; Rinzler, A. G.; Dai, H.; Hafner, J. H.; Bradley, R. K.; Boul, P. J.; Lu, A.; Iverson, T.; Shelimov, K.; Huffman, C. B.; Rodriguez-Macias, F.; Shon, Y.-S.; Lee, T. R.; Colbert, D. T.; Smalley, R. E. *Science* **1998**, *280*, 1253–1256.
- (12) Maurin, G.; Stepanek, I.; Bernier, P.; Colomer, J. F.; Nagy, J. B.; Henn, F. *Carbon* **2001**, *39*, 1273.
- (13) Yudasaka, M.; Zhang, M.; Jabs, C.; Iijima, S. *Appl. Phys. A* **2000**, *71*, 449.
- (14) Zorbas, V.; Ortiz-Acevedo, A.; Dalton, A. B.; Yoshida, M. M.; Dieckmann, G. R.; Draper, R. K.; Baughman, R. H.; Jose-Yacamán, M.; Musselman, I. H. *J. Am. Chem. Soc.* **2004**, *126*, 7222–7227.
- (15) Islam, M. F.; Rojas, E.; Bergey, D. M.; Johnson, A. T.; Yodh, A. G. *Nano Lett.* **2003**, *3*, 269–273.
- (16) Bronikowski, M. J.; Willis, P. A.; Colbert, D. T.; Smith, K. A.; Smalley, R. E., *J. Vac. Sci. Technol. A* **2001**, *19*, 1800–1805.
- (17) Lebedkin, S.; Schweiss, P.; Renker, B.; Malik, S.; Hennrich, F.; Neumaier, M.; Stoermer, C.; Kappes, M. M. *Carbon* **2002**, *40*, 417–423.
- (18) Guo, T.; Nikolaev, P.; Thess, A.; Colbert, D. T.; Smalley, R. E. *Chem. Phys. Lett.* **1995**, *243*, 49–54.
- (19) Hennrich, F.; Wellmann, R.; Malik, S.; Lebedkin, S.; Kappes, M. M.; *Phys. Chem. Chem. Phys.* **2003**, *5*, 178–183.
- (20) Telg, H.; Maultzsch, J.; Reich, S.; Hennrich, F.; Thomsen, C. *Phys. Rev. Lett.* **2004**, *93*, 177401.1–4.
- (21) Bachilo, S. M.; Strano, M. S.; Kittrell, C.; Hauge, R. H.; Smalley, R. E.; Weisman, R. B. *Science* **2002**, *298*, 2361–2366.
- (22) Zhong, Q.; Inniss, D.; Kjoller, K.; Elings, V. B. *Surf. Sci. Lett.* **1993**, *290*, L688.
- (23) Pang, G. K. H.; Baba-Kishi, K. Z.; Patel, A. *Ultramicroscopy* **2000**, *81*, 35.
- (24) Lebedkin, S.; Arnold, K.; Hennrich, F.; Krupke, R.; Renker, B.; Kappes, M. M. *New J. Phys.* **2003**, *5*, 140.1–11.
- (25) Reich, S.; Thomsen, C.; Robertson, J. *Phys. Rev. Lett.* **2005**, *95*, 077402.1–4.
- (26) Odell, J. A.; Keller, A. *J. Polym. Sci., Part B* **1986**, *24*, 1889–1916.
- (27) Kuijpers, M. W. A.; Iedema, P. D.; Kemmere, M. F.; Keurentjes, J. T. F. *Polymers* **2004**, *45*, 6461–6467.
- (28) Agarwal, U. S. *e-Polymers* **2002**, *14*, 1–15.
- (29) Keller, J. B.; Rubinow, S. I. *J. Fluid Mech.* **1976**, *75*, 705–714.
- (30) Natsuki, T.; Endo, M. *Appl. Phys. A* **2005**, *80*, 1463–1468.
- (31) Walther, J. H.; Werder, T.; Jaffe, R. L.; Koumoutsakos, P. *Phys. Rev. E* **2004**, *69*, 062201.
- (32) Kuijpers, M. W. A.; van Eck, D.; Kemmere, M. F.; Keurentjes, J. T. F. *Science* **2002**, *298*, 1969–1971.